Journal of Power Sources 196 (2011) 9625–9630

Contents lists available at ScienceDirect

Journal of Power Sources

journal homepage: www.elsevier.com/locate/jpowsour

Enhanced electrochemical performance of porous NiO–Ni nanocomposite anode for lithium ion batteries

Xifei Li, Abirami Dhanabalan, Chunlei Wang*

Department of Mechanical and Materials Engineering, Florida International University, Miami, FL 33174, USA

ARTICLE INFO

Article history:
Received 2 May 2011
Received in revised form 27 June 2011
Accepted 28 June 2011
Available online 5 July 2011

Keywords:
Porous
NiO–Ni
Nanocomposite
Anode
Lithium ion batteries
Cycle performance
Rate capability

ABSTRACT

The nickel foam-supported porous NiO–Ni nanocomposite synthesized by electrostatic spray deposition (ESD) technique was investigated as anodes for lithium ion batteries. This anode was demonstrated to exhibit improved cycle performance as well as good rate capability. Ni particles in the composites provide a highly conductive medium for electron transfer during the conversion reaction of NiO with Li^+ and facilitate a more complete decomposition of Li_2O during charge with increased reversibility of conversion reaction. Moreover, the obtained porous structure is benefical to buffering the volume expansion/constriction during the cycling.

1. Introduction

Carbon-based materials like graphite have been employed as anodes in commercial available lithium ion batteries (LIBs) since 1991 due to their high deliverable operation potential, good electronic conductivity, high Li^+ chemical diffusion coefficient and low volume changes during Li^+ intercalation/de-intercalation [1]. However, their limited capacities (theoretical capacity of graphite is 372 mAh g^{-1}) could not match the urgent need in recent high energy density and power density rechargeable LIB applications for hybrid and plug-in hybrid electric vehicles [2,3]. On the one hand, various carbon nanostructures, such as porous carbon, are still under intensive development because they can provide fast kinetics and are structural stable during charge/discharge [4]. On the other hand, some new promising anode materials, like rock salt structured transition-metal oxides (M_xO_y, M = Ni, Co, Cu, etc.) [5,6], Sn [7], Si [8], and SnO_2 [9], recently draw tremendous interest due to their higher theoretical capacities than graphite anode. Si anode has the highest theoretical energy capacity (4200 mAh g^{-1}), but the large volume change (>300%) during lithium alloying/de-alloying results in poor cyclability [8]. Transition metal oxides have long been disregarded as possible reversible anode materials for LIBs because they have no intercalation/de-intercalation sites in their crystal structures, furthermore, they are not available to form alloys with lithium during charge and discharge [10]. Recently, Tarascon and co-workers revisited this issue and proposed the possibility of using the transition metal oxide materials as anodes in LIBs [5,6]. To distinguish such anodes from the other types regarding the charge–discharge mechanism with lithium, conversion reaction mechanism has been introduced [11–13], which is different from classical Li^+ intercalation/de-intercalation in graphite or alloying/de-alloying reactions of metallic or semimetallic anodes (such as Sn, Ge, Si, etc.) with lithium [14].

Among transition metal oxides, NiO anode shows the high theoretical capacity up to 718 mAh g^{-1}. Its density, 6.81 g cm^{-3}, is much higher than that of graphite, 2.268 g cm^{-3}, which results in volumetric energy density of NiO anode as about 5.8 times as theoretical value of graphite. Therefore, NiO has been regarded as one of the promising anodes for LIBs. However, NiO is an antiferromagnetic semiconductor with a wide band gap of ~3.6 eV and low electrical conductivity (less than 10^{-13} Ω^{-1} cm^{-1} at room temperature) [15,16]. Recently, it was reported that nanostructured NiO–carbon composites show better capacity retention than pristine NiO due to the introduction of carbon with good electrical conductivity [17–19]. Carbon with the low density in the composites occupying extra space limits the specific volumetric capacity of NiO anode. To circumvent this challenge, some metals like Au and Ag as additives were employed to create transition metal oxides–metal composite [20–23]. The reaction of NiO anode with Li^+ leads to the formation of metallic Ni and Li_2O nanoparticles accompanied with the large volume expansion/constriction for the conversion reaction. An "earthquake" created in the anode electrode during conversion

* Corresponding author. Tel.: +1 305 348 1217.
E-mail address: wangc@fiu.edu (C. Wang).

0378-7753/$ – see front matter © 2011 Elsevier B.V. All rights reserved.
doi:10.1016/j.jpowsour.2011.06.097

reaction [24] is another drawback affecting the application of NiO anode for LIBs because it causes the pulverization and degradation of NiO anode, resulting in serious capacity degradation and poor cycling performance [25–28]. One effective method to alleviate the problem is to create porous structure to buffer the volume change upon cycles [29–31].

In this work, porous NiO–Ni nanocomposite was deposited on porous nickel foam by electrostatic spray deposition (ESD) technique. The specific surface area of nickel foam is much higher than that of conventional thin foil, thus depositing anode materials on a nickel foam substrate is an attractive method to prepare anode electrodes for LIBs [32,33]. On the one hand, during the reversible reaction of NiO with Li^+, the conversion reaction mechanism involves the reduction and oxidation of Ni nanoparticles, thus the existence of nanoscale Ni in the NiO–Ni nanocomposite has the possibility to facilitate the decomposition of Li_2O increasing the columbic efficiency of NiO anode. On the other hand, as-prepared porous Ni foam supported-porous NiO–Ni composite was employed as anode materials for LIBs without conductive agent and binder, thus the energy density of LIBs can be increased while the anode resistances are efficiently reduced. Furthermore, the special porous structure can effectively reduce the agglomeration of nanoscale particles during cycling. It is expected that porous Ni foam supported-porous NiO–Ni composite can improve the electrochemical performance as anode for LIBs.

2. Experimental

NiO–Ni composite anode was synthesized by using a vertical ESD setting-up schematically illustrated in Fig. 1. Nickel acetate was dissolved in the 80 vol% of butyl carbitol and 20 vol% of ethanol as precursor solution. The precursor solution was atomized at a high DC voltage of 4.0–6.0 kV. Commercially available porous nickel foam (Changsha Lyrun Material Co., LTD) was used as the substrate due to its high surface area. The nozzle-to-substrate distance was set to be 40–50 mm. The deposition temperature was controlled at 300 °C. During the ESD deposition, the precursor solution was atomized to an aerosol under the static electric force by the high voltage between the substrate and the tip of nozzle. And then the aerosol reached the heated substrate, where the NiO–Ni composite was formed on a nickel foam substrate. The samples before and after ESD deposition were weighed by a balance with an accuracy of 0.01 mg to calculate the weight of the deposited NiO on nickel foam substrate.

X-ray diffraction (XRD) was carried out using a Siemens D5000 from 20° to 90° with Cu K_α radiation (λ = 1.54056 nm). Scanning electron microscopy (SEM) (JEOL JSM-6330F) with the energy dispersive X-ray analysis (EDX) was used to observe the surface morphology, confirm the surface uniformity and measure the NiO content in as-prepared NiO–Ni nanocomposites. The Raman spectra were recorded on an RFS-100 Bruker FT-spectrometer using an Nd:YAG laser with an excitation wavelength of 1064 nm. Each spectrum was the average of 60 repeated measurements, with 150 scans at a resolution of 2 cm^{-1}.

The CR-2032-type coin cells were assembled inside an argon atmosphere glove box with moisture and oxygen levels below 1 ppm. NiO–Ni composite was used as working electrode, and lithium foil as counter electrode and reference electrode. The separator film was Celgrad 2400. The liquid electrolyte was 1 M lithium bis(perfluoroethylsulfonyl)imide dissolved in ethylene carbonate (EC): diethyl carbonate (DEC): ethyl methyl carbonate (EMC) in a 1:1:1 volume ratio. Cyclic voltammetry (CV) tests were performed at a scan rate of 0.1 mV s^{-1} over a potential range of 0.02–3.00 V (versus Li^+/Li) using a Versatile Multichannel Potentiostat 3/Z (VMP3). Charge–discharge characteristics were tested galvanostatically between 0.02 and 3.00 V (versus Li/Li^+) at room temperature by a Neware Battery Test System (NEWARE Technology Limited, China). In the charge/discharge tests, the reduction of the NiO–Ni composite is expressed as "discharge" to define the Li^+ insertion process.

3. Results and discussions

In this research, XRD technique was carried out in order to examine the product deposited by the ESD method. The XRD pattern of obtained film is shown in Fig. 2a. Five obvious diffraction

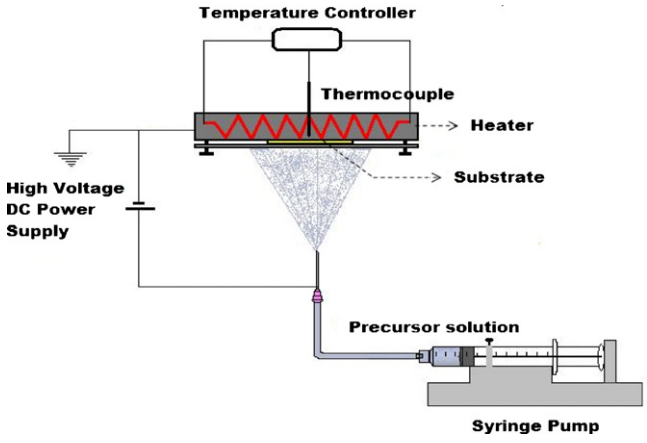

Fig. 1. Schematic diagram of electrostatic spray deposition technique.

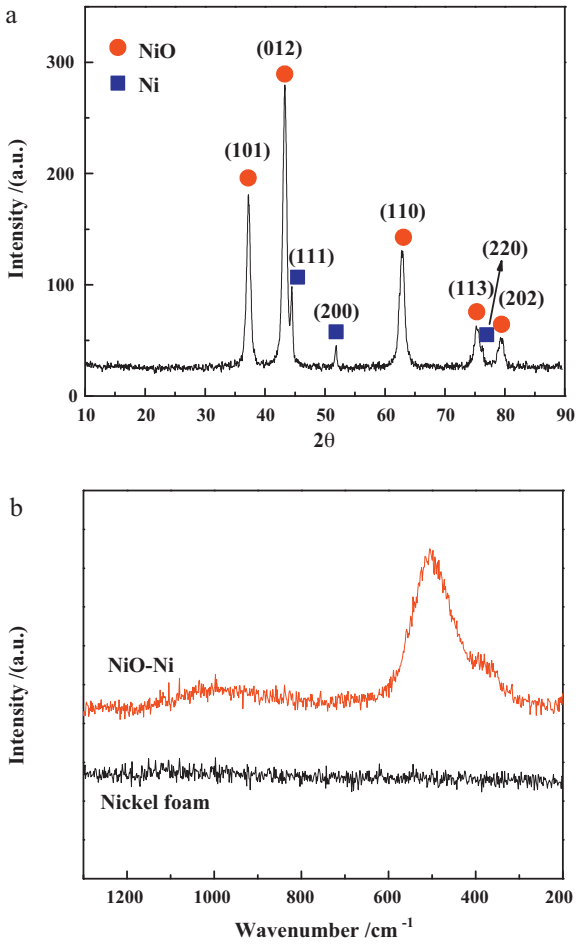

Fig. 2. (a) A typical XRD spectrum and (b) Raman spectra of NiO–Ni composite anode compared to bare Ni foam substrate.

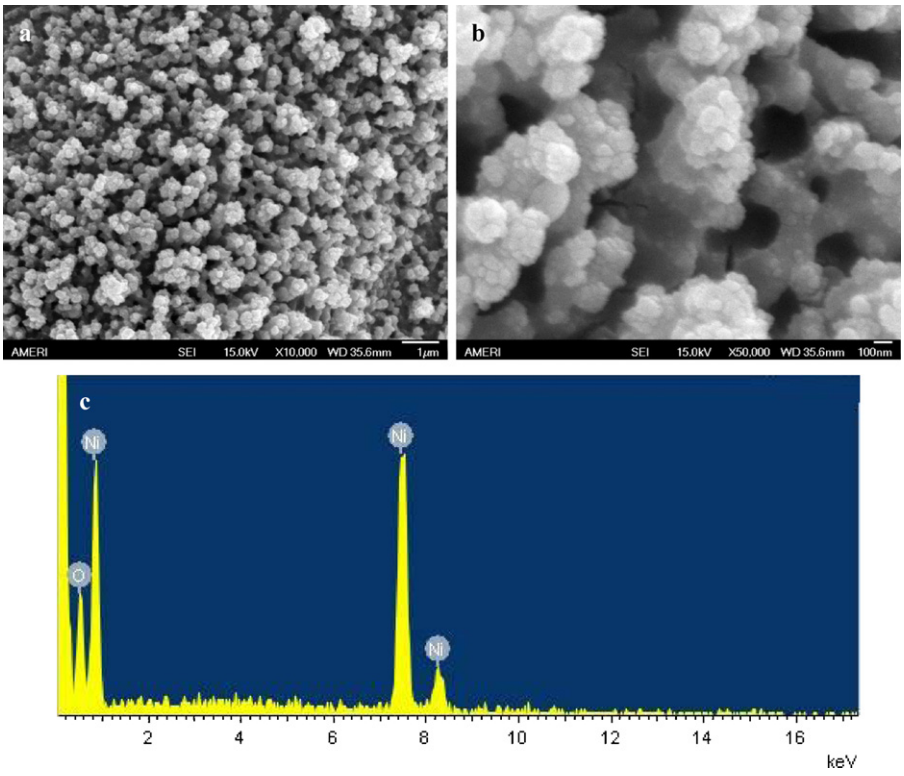

Fig. 3. Typical SEM images (a, b) and an energy dispersive X-ray (EDX) spectrum (c) of the NiO–Ni nanocomposite anode.

peaks located at 37.2°, 43.3°, 62.8°, 75.4° and 79.3° well agree with cubic structure NiO (1 0 1), (0 1 2), (1 10), (1 1 3) and (2 0 2) plane, respectively (JCPDS 44-1159). Furthermore, three Ni planes, (1 1 1), (2 0 0), and (2 2 0), were observed to locate at 44.5°, 51.9° and 76.4°, respectively (JCPDS 4-850). It can be concluded through the XRD result that NiO-Ni composites were formed after the ESD process. NiO formation was further confirmed by Raman spectra shown in Fig. 2b. There are no Raman peaks observed for Ni since it has no active vibrational Raman mode. NiO–Ni composite shows an obvious and broad peak in the Raman spectrum located at about 510 cm^{-1} that can be assigned to the vibration modes of Ni–O bonds [34], which indicates the NiO existence in the NiO–Ni composite. EDX spectrum of NiO–Ni composite is shown in Fig. 3c. Specified peaks corresponding to Ni and O can be clearly observed. Based on the atom ratio (57:43) of Ni and O, NiO content was roughly calculated to be 79.6% in the NiO–Ni composite. It was reported that nickel acetate can decompose into NiO and Ni under air atmosphere [35–38]. As it was reported by Hussein et al. [35], nickel acetate decomposes through two exothermic processes: (1) solid phase NiO and gas phase acetone and CO_2 are formed first; (2) then some of NiO is reduced to Ni through an endothermic process, most likely involving a CO-reduction step, thereby, the decomposition of nickel acetate results in a mixture of NiO and Ni. However, further study needs to be done to accurately assess the composition of the NiO–Ni composite.

During the ESD process, as shown in Fig. 1, the high potential at the nozzle tip induced the surrounding air ionized, resulting in a large amount of positive ions (e.g., O^+, O^{2+}) with high-velocity. These ions then charged the $Ni(OAC)_2$ solution by their bombardment in the surrounding area of the nozzle outlet when they moved towards the substrate. Thereby the $Ni(OAC)_2$ solution was atomized and dispersed into tiny droplets with the help of electrostatic repulsion force. The resultant droplets moved towards the substrate due to the effect of the electrical field. When the droplets hit the substrate surface, part of the droplets had enough time to spread on the heated substrate before the solvent completely evaporated. The local temperature at the edge of a landed droplet was higher than that of in the centre as soon as the heat transferred from the substrate to the droplets, which resulted in the faster solvent evaporation at the edges. Simultaneously, both the evaporation of the solvent and the decomposition of $Ni(OAC)_2$ occurred at the edges. There is an inhomogeneous concentration profile in the droplets inducing the solution in the middle flowing towards the edge [39]. Further evaporation of the solvent and the decomposition of $Ni(OAC)_2$ at the edges can form porous structure as shown in Fig. 3a and b. The porous feature was with a size of about 100-300 nm. Because the substrate temperature was 300 °C higher than the boiling point (231 °C) of butyl carbitol, some particles were likely produced during the flight of the droplets to the nickel foam substrate. These particles arrived at the substrate and attached to the formed porous structure.

The electrochemical property of NiO–Ni nanocomposite as anode for LIBs was examined by cyclic voltammetry. Fig. 4a presents the CV curves of NiO–Ni anode at the 1st, 2nd, 10th, and 20th scanning cycles. In the first cathodic scan, a reduction peak related to the decomposition of NiO into Ni ($NiO + 2Li^+ + 2e^- \rightarrow Ni + Li_2O$) was observed at around 0.2 V. The resultant Ni particles might have the sizes of several nanometers [5,6,40,41], resulting in the reduction potential shifts to 1.2 V in subsequent cathodic scan [42]. The oxidation peaks, resulting from the reactions where nanosized Ni is re-oxidized to nanosized NiO ($Ni + Li_2O \rightarrow NiO + 2Li^+ + 2e^-$) at different cycles [43], show similar potentials at different cycles. It is confirmed that the reversible electrochemical reaction between Li^+ and NiO–Ni nanocomposite anode from the CV results.

Fig. 4b shows the charge and discharge voltage profiles as a function of the specific capacity for the NiO–Ni composite anode at a current density of 286 mA g^{-1} at the 1st, 2nd, 50th and 100th cycles, respectively. In the first discharge (Li^+ insertion), the potential of NiO–Ni anode rapidly falls, followed by an obvious plateau at about 0.5 V corresponding to the decomposition of NiO into Ni. It delivered a discharge capacity of 503 mAh g^{-1} and a reversible

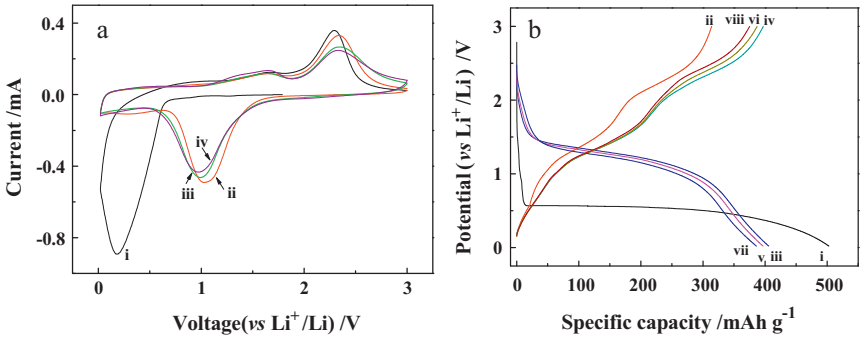

Fig. 4. (a) CV curves of the NiO–Ni composite anode at a scan rate of 0.1 mV s^{-1}: (i) the first discharge, (ii) the second scan, (iii) the 10th scan, and (iv) the 20th scan; (b) charging–discharging curves for the NiO–Ni/Li half cell cycled between 0.02 and 3 V at a current density of 286 mA g^{-1}: (i) the first discharge, (ii) the first charge, (iii) the second discharge, (iv) the second charge, (v) the 50th discharge, (vi) the 50th charge, (vii) the 100th discharge, and (viii) the 100th charge, respectively.

charge (Li^+ deinsertion) capacity of 314 mAh g^{-1} in the first cycle. The irreversible capacity is mainly ascribed to the formation of the solid electrolyte interphase (SEI) film on the surface of NiO anode [44]. As it was reported for NiO anode in many Refs. [6,42,45,46], the second discharge profile is different from the first one. In the second discharge, the plateau was distinctly higher and more sloped than the main feature of the first discharge, which indicates that the Li^+ insertion in the second cycle is easier and is the feature of a single phase reaction. Under the electrochemical reaction in the first discharge process, NiO can be changed into the fine particles with a size of several nanometers [5,6,40,41]. Therefore, in the subsequent discharge, the related reaction potential shifts to higher voltage due to the fast kinetic of the nanomaterials. It is worth noting that the second charge profile is very similar to the first charge. From the second cycle, the electrochemical reaction of the electrode is improved reversibly. However, an obvious voltage hysteresis is still observed between discharge and charge due to the nature of a conversion reaction. The reversible discharge and charge capacities at the 50th cycle are 397 mAh g^{-1} and 387 mAh g^{-1}, respectively. Its columbic efficiency is about 97.5% similar to that of the 100th cycle. In the NiO–Ni nanocomposites, Ni has no contribution for energy capacity; as a consequence, the Ni existence decreases the specific capacity of NiO anode for lithium ion batteries.

The Li^+ storage performance of NiO–Ni nanocomposite anode for LIBs was evaluated via the galvanostatic charge/discharge cycling. At a current density of 286 mA g^{-1} in the voltage window of 0.02–3.00 V, the relationship of reversible Li^+ storage capacity vs. cycle number is shown in Fig. 5a. Obviously, the NiO–Ni nanocomposite electrode presents good cyclability during charge/discharge process, with high capacity retention of 95.1% at 100 cycles. The

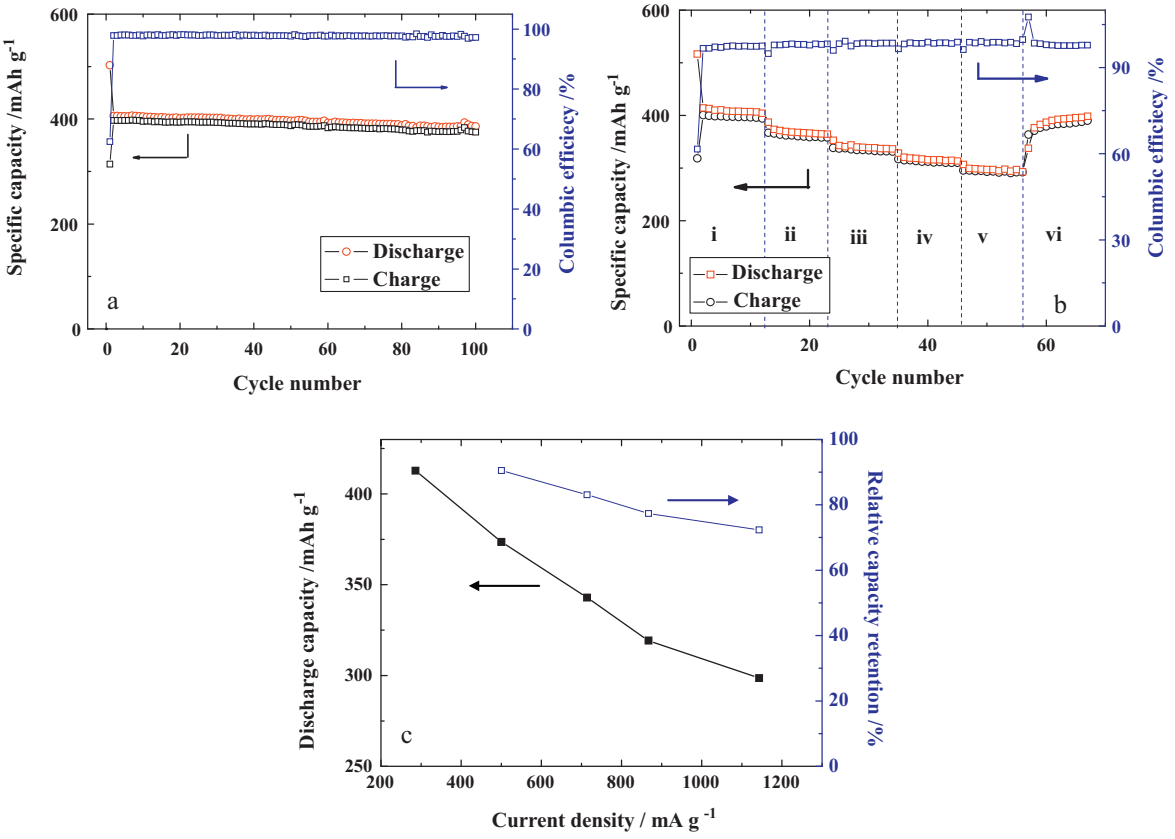

Fig. 5. (a) Specific capacity and columbic efficiency of NiO–Ni composite anode as a function of the cycle number at a current density of 286 mA g^{-1} at a voltage range of 0.02–3.00 V at the room temperature; (b) rate capability of NiO–Ni composite anode at various current densities (mA g^{-1}): (i) 286, (ii) 500, (iii) 714, (iv) 867, (v) 1143, and (vi) 286, respectively; (c) discharge capacity and relative capacity retention of NiO–Ni composite anode as a function of current density from 286 to 1143 mA g^{-1}.

rate capability is an important parameter of LIBs for many applications such as electric vehicles, which requires fast discharge/charge rate [47]. The rate capability of NiO–Ni composite anode at various current densities from 286 mA g^{-1} to 1143 mA g^{-1} in a voltage window of 0.02–3.00 V at ambient temperature is presented in Fig. 5b. NiO–Ni composite anode shows relatively steady capacity change at different current density, even at the high current density of 1143 mA g^{-1}. The charge/discharge capacities decrease with the increase of current density, which is caused by lower Li^+ diffusion rate in the NiO particles. By comparing the discharge capacity of the second cycle at various current densities, NiO–Ni composite anode is found to deliver 90.5% capacity retention at 500 mA g^{-1}, 83.1% at 714 mA g^{-1}, 77.3% at 867 mA g^{-1}, and 72.3% at 1143 mA g^{-1} (relative to the capacity at 286 mA g^{-1}), respectively (Fig. 5c). After 56 charge/discharge cycles under various current densities, NiO–Ni composite could still work pretty stably and reversibly. It delivers the discharge capacity of 399 mAh g^{-1} in the 67th cycle, maintaining 98.8% of the discharge capacity recorded at the 12th cycle at the same current density. All these results demonstrated that NiO–Ni is a very promising anode for LIBs showing excellent rate capability.

For the pristine NiO anode, the Ni nanoparticles can only result from the decomposition of the starting NiO during the discharge ($NiO + 2Li^+ + 2e^- \rightarrow Ni + Li_2O$). Most of these Ni nanoparticles can convert back to NiO during the charge process. For the NiO–Ni composite, as the NiO particles are decorated with nanoscale Ni particles, some active Ni particles can be present in the composite anodes during the whole discharge–charge cycle. Highly dispersed Ni particles in the NiO–Ni composite have some catalytic effect ($Ni + Li_2O \rightarrow NiO + 2Li^+ + 2e^-$). During the charge process, the extra active Ni particles among the resultant Li_2O particles can facilitate more complete decomposition of Li_2O [22,48]. It is well known that the poor electrical conductivity of transition metal oxides is a big obstacle for their application as anodes for LIBs. Metallic Ni particles in the NiO–Ni composite can provide a highly conductive medium for electron transfer during the conversion reaction of NiO with Li^+. As a consequence, our porous NiO–Ni nanocomposites have effectively improved the reversibility. On the other side, as-prepared porous structure can buffer the large volume expansion/constriction due to the "earthquake" created in the transition metal oxide anode during the charge/discharge process [24,30]. Furthermore, both porous nickel foam and porous NiO–Ni ensure a large contact area between active material and the electrolyte with shorter Li^+ diffusion length [49,50]. Therefore, our porous NiO–Ni nanocomposite anode has been demonstrated with effectively improved cycle performance and rate capability. Further in situ work needs to be done to provide more information on if the Ni nanoparticles are uniformly dispersed in the composite or not and how they buffer the volume change during cycling.

4. Conclusion

In this work, porous nickel foam-supported porous NiO–Ni nanocomposite anodes have been successfully synthesized by the ESD technique. NiO–Ni anode shows the porous structure with typical pore size of about 100–300 nm attached with nanoparticles at sizes of 40–60 nm. Our results demonstrated that NiO–Ni nanocomposite anode shows good cyclability, good rate capability, and high capacity retention of 95.1% after 100 cycles. The enhanced electrochemical performance can be attributed to extra nanoscaled Ni particles as highly conductive medium and catalyst facilitating more complete decomposition of Li_2O during charge. Also the porous NiO–Ni nanocomposite can buffer the large volume expansion/constriction during charge/discharge process.

Acknowledgements

Authors would like to acknowledge the Air Force Office of Scientific Research (AFOSR FA9550-08-1-0287), American Chemical Society (Petroleum Research Fund, 49301-0N110), and the Advanced Materials Engineering Research Institute (AMERI) facility at Florida International University.

References

[1] M. Endo, C. Kin, K. Nishimura, T. Fujino, K. Miyashita, Carbon 38 (2000) 183.
[2] M. Winter, J.O. Besenhard, M.E. Spahr, P. Novak, Adv. Mater. 10 (1998) 725.
[3] W.V. Schalkwijk, B. Scrosati, Advances in lithium-ion batteries, Kluwer Academic/Plenum Publishers, New York, USA, 2002, p. 433.
[4] N.A. Kaskhedikar, J. Maier, Adv. Mater. 21 (2009) 2664.
[5] P. Poizot, S. Laruelle, S. Grugeon, L. Dupont, J.M. Tarascon, Nature 407 (2000) 496.
[6] P. Poizot, S. Laruelle, S. Grugeon, L. Dupont, J.M. Tarascon, J. Power Sources 97–98 (2001) 235.
[7] W.M. Zhang, J.S. Hu, Y.G. Guo, S.F. Zheng, L.S. Zhong, W.G. Song, L.J. Wan, Adv. Mater. 20 (2008) 1160.
[8] H. Ma, F. Cheng, J.Y. Chen, J.Z. Zhao, C.S. Li, Z.L. Tao, J. Liang, Adv. Mater. 19 (2007) 4067.
[9] H.X. Zhang, C. Feng, Y.C. Zhai, K.L. Jiang, Q.Q. Li, S.S. Fan, Adv. Mater. 21 (2009) 2299.
[10] S. Laruelle, S. Grugeon, P. Poizot, M. Dolle, L. Dupont, J.M. Tarascon, J. Electrochem. Soc. 149 (2002) A627.
[11] R. Malini, U. Uma, T. Sheela, M. Ganesan, N.G. Renganathan, Ionics 15 (2009) 301.
[12] M.V. Reddy, T. Yu, C.H. Sow, Z.X. Shen, C.T. Lim, G.V. Subba Rao, B.V.R. Chowdari, Adv. Funct. Mater. 17 (2007) 2792.
[13] J.M. Tarascon, M. Armand, Nature 414 (2001) 359.
[14] Y. Kim, H. Hwang, C.S. Yoon, M.G. Kim, J. Cho, Adv. Mater. 19 (2007) 92.
[15] D. Adler, J.J. Feinleib, Phys. Rev. B 2 (1970) 3112.
[16] P. Lukenheimer, A. Wide, C.R. Ottermann, K. Bange, Phys. Rev. B 44 (1991) 5927.
[17] X.H. Huang, J.P. Tu, C.Q. Zhang, J.Y. Xiang, Electrochem. Commun. 9 (2007) 1180.
[18] M.M. Rahman, S.L. Chou, C. Zhong, J.Z. Wang, D. Wexler, H.K. Liu, Solid State Ionics 180 (2010) 1646.
[19] X.H. Huang, J.P. Tu, C.Q. Zhang, X.T. Chen, Y.F. Yuan, H.M. Wu, Electrochim. Acta 52 (2007) 4177.
[20] K.T. Nam, D.W. Kim, P.J. Yoo, C.Y. Chiang, N. Meethong, P.T. Hammond, Y.M. Chiang, A.M. Belcher, Science 312 (2006) 885.
[21] X.H. Huang, J.P. Tu, Z.Y. Zeng, J.Y. Xiang, X.B. Zhao, J. Electrochem. Soc. 155 (2008) A438.
[22] X.H. Huang, J.P. Tu, B. Zhang, C.Q. Zhang, Y. Li, Y.F. Yuan, H.M. Wu, J. Power Sources 161 (2006) 541.
[23] P.L. Taberna, S. Mitra, P. Poizot, P. Simon, J.M. Tarascon, Nat. Mater. 5 (2006) 567.
[24] C. Villevieille, M. Boinet, L. Monconduit, Electrochem. Commun. 12 (2010) 1336.
[25] S.F. Zheng, J.S. Hu, L.S. Zhong, W.G. Song, L.J. Wan, Y.G. Guo, Chem. Mater. 20 (2008) 3617.
[26] L. Wang, H.W. Xu, P.C. Chen, D.W. Zhang, C.X. Ding, C.H. Chen, J. Power Sources 193 (2009) 846.
[27] J. Hu, H. Li, X.J. Huang, Electrochem. Solid-State Lett. 8 (2005) A66.
[28] L. Liu, Y. Li, S.M. Yuan, M. Ge, M.M. Ren, C.S. Sun, Z. Zhou, J. Phys. Chem. C 114 (2010) 251.
[29] H. Kim, B. Han, J. Choo, J. Cho, Angew. Chem. Int. Ed. 120 (2008) 10305.
[30] H. Kim, J. Cho, J. Mater. Chem. 18 (2008) 771.
[31] J. Cho, J. Mater. Chem. 20 (2010) 4009.
[32] F. Gillot, S. Boyanov, L. Dupont, M.L. Doublet, M. Morcrette, L. Monconduit, J.M. Tarascon, Chem. Mater. 17 (2005) 6327.
[33] Y. Yu, C.H. Chen, J.L. Shui, S. Xie, Angew. Chem. Int. Ed. 44 (2005) 7085.
[34] N. Dharmaraj, P. Prabu, S. Nagarajan, C.H. Kim, J.H. Park, H.Y. Kim, Mater. Sci. Eng. B 128 (2006) 111.
[35] G.A.M. Hussein, A.K.H. Nohman, K.M.A. Attyia, J. Therm. Anal. 42 (1994) 1155.
[36] M.A. Mohamed, S.A. Halawy, M.M. Ebrahim, J. Anal. Appl. Pyrol. 27 (1993) 109.
[37] J.C. De Jesus, I. Gonzalez, A. Quevedo, T. Puerta, J. Mol. Catal. A: Chem. 228 (2005) 283.
[38] A.K. Galwey, S.G. Mckee, T.R.B. Mitchell, M.E. Brown, A.F. Bean, React. Solids 6 (1998) 173.
[39] Y.Z. Jiang, Y. Yu, W.P. Sun, C.H. Chen, G.Y. Meng, J.F. Gao, J. Electrochem. Soc. 154 (2007) E107.
[40] S. Grugeon, S. Laruelle, L. Dupont, J.M. Tarascon, Solid State Sci. 5 (2003) 895.
[41] S. Grugeon, S. Laruelle, R. Herrera-Urbina, L. Dupont, P. Poizot, J.M. Tarascon, J. Electrochem. Soc. 148 (2001) A285.
[42] B. Varghese, M.V. Reddy, Y.W. Zhu, S.L. Chang, C.H. Teo, G.V.S. Rao, B.V.R. Chowdari, A.T.S. Wee, C.T. Lim, C.H. Sow, Chem. Mater. 20 (2008) 3360.
[43] P. Poizot, S. Laruelle, S. Grugeon, J.M. Tarascon, J. Electrochem. Soc. 149 (2002) A1212.

[44] A.L.M. Reddy, M.M. Shaijumon, S.R. Gowda, P.M. Ajayan, Nano Lett. 9 (2009) 1002.
[45] C.H. Xu, J. Sun, L. Gao, J. Power Sources 196 (2011) 5138.
[46] J. Zhong, X.L. Wang, X.H. Xia, C.D. Gu, J.Y. Xiang, J. Zhang, J.P. Tu, J. Alloy Compd. 509 (2011) 3889.
[47] Y.g. Li, B. Tan, Y.Y. Wu, Nano Lett. 8 (2008) 265.
[48] C.Q. Zhang, J.P. Tu, Y.F. Yuan, X.H. Huang, X.T. Chen, F. Mao, J. Electrochem. Soc. 154 (2007) A65.
[49] X.F. Li, A. Dhanabalan, K. Bechtold, C.L. Wang, Electrochem. Commun. 12 (2010) 1222.
[50] Q. Wang, R. Gao, J.H. Li, Appl. Phys. Lett. 90 (2007) 143107.